

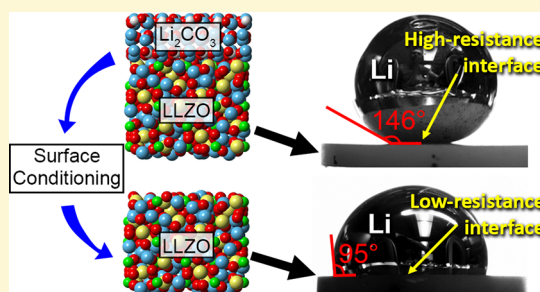
Surface Chemistry Mechanism of Ultra-Low Interfacial Resistance in the Solid-State Electrolyte $\text{Li}_7\text{La}_3\text{Zr}_2\text{O}_{12}$

Asma Sharafi,[†] Eric Kazyak,[†] Andrew L. Davis,[†] Seungho Yu,[†] Travis Thompson,[†] Donald J. Siegel,^{†,‡,§,⊥} Neil P. Dasgupta,^{*,†,⊥} and Jeff Sakamoto^{*,†,‡,§}

[†]Department of Mechanical Engineering, [‡]Department of Materials Science and Engineering, [§]Michigan Energy Institute, and [⊥]Applied Physics Program, University of Michigan, Ann Arbor, Michigan 48109, United States

S Supporting Information

ABSTRACT: The impact of surface chemistry on the interfacial resistance between the $\text{Li}_7\text{La}_3\text{Zr}_2\text{O}_{12}$ (LLZO) solid-state electrolyte and a metallic Li electrode is revealed. Control of surface chemistry allows the interfacial resistance to be reduced to $2\ \Omega\ \text{cm}^2$, lower than that of liquid electrolytes, without the need for interlayer coatings. A mechanistic understanding of the origins of ultra-low resistance is provided by quantitatively evaluating the linkages between interfacial chemistry, Li wettability, and electrochemical phenomena. A combination of Li contact angle measurements, X-ray photoelectron spectroscopy (XPS), first-principles calculations, and impedance spectroscopy demonstrates that the presence of common LLZO surface contaminants, Li_2CO_3 and LiOH , result in poor wettability by Li and high interfacial resistance. On the basis of this mechanism, a simple procedure for removing these surface layers is demonstrated, which results in a dramatic increase in Li wetting and the elimination of nearly all interfacial resistance. The low interfacial resistance is maintained over one-hundred cycles and suggests a straightforward pathway to achieving high energy and power density solid-state batteries.



INTRODUCTION

A transition from a fossil fuel-based economy to one based on renewable resources has sparked interest in the development of energy storage devices with higher energy density, enhanced safety, and reduced cost.¹ Li-ion batteries (LIBs) represent a promising technology for near-term energy storage needs; however, for emerging applications such as electric vehicles, a step-change increase in battery performance is highly desirable.

Toward this goal, specific energies and energy densities exceeding $500\ \text{Wh}\ \text{kg}^{-1}$ and $1000\ \text{Wh}\ \text{l}^{-1}$, respectively, with costs less than $\$100\ \text{kWh}^{-1}$, could be achieved through the development of solid-state electrolytes (SSE).² The garnet-type SSE, based on the nominal formula $\text{Li}_7\text{La}_3\text{Zr}_2\text{O}_{12}$ (LLZO), is unique in that it is a fast Li-ion conductor ($1\ \text{mS}\ \text{cm}^{-1}$ at 298 K), exhibits sufficient mechanical properties,³ and is also chemically and electrochemically stable against metallic Li.⁴ Despite these promising attributes, additional challenges must be overcome before solid-state batteries (SSBs) based on LLZO are viable. Demonstrating low Li–LLZO interfacial resistance ($R_{\text{Li-LLZO}}$) is a critical milestone along the path to commercialization. While several studies have characterized $R_{\text{Li-LLZO}}$, nearly all report values significantly higher than conventional LIBs employing liquid electrolytes ($\sim 10\ \Omega\ \text{cm}^2$).^{5–7} Thus, strategies to reduce $R_{\text{Li-LLZO}}$ to values comparable to, or lower than, LIBs are needed.

Recently, coating of the LLZO surface was investigated to reduce $R_{\text{Li-LLZO}}$. For example, Tsai et al. sputter coated Au on LLZO and demonstrated a $R_{\text{Li-LLZO}}$ of $58\ \Omega\ \text{cm}^2$ at $25\ ^\circ\text{C}$.⁸ It

was hypothesized that the Au coating provided uniform conductivity at the Li–LLZO interface, lowering $R_{\text{Li-LLZO}}$. In related work, Han et al. suggested that an Al_2O_3 coating could reduce $R_{\text{Li-LLZO}}$, but the interface resistance was not directly measured using electrochemical impedance spectroscopy (EIS); instead, $R_{\text{Li-LLZO}}$ was extrapolated from DC cycling data, making it difficult to quantitatively interpret efficacy. The authors attributed the reduction in $R_{\text{Li-LLZO}}$ to enhanced Li wettability of the LLZO surface.⁹ However, the mechanism of how surface modifications led to improved performance has not been explicitly determined.

Thus, while the use of coatings can in some instances improve performance, the underlying physical and chemical mechanisms that control interfacial resistance are not well understood, which has limited interfacial chemical modification studies to largely empirical observations. A mechanistic understanding of the coupling between interfacial chemistry, Li wettability, and interfacial resistance would accelerate the rational design of engineered interfaces having low $R_{\text{Li-LLZO}}$. Such an understanding would also address the question of whether low interfacial resistance could be achieved *without* the need for coatings, as these add additional processing steps, create additional interfaces, and could compromise cycle life if the coating does not maintain integrity upon cycling.

Received: July 18, 2017

Revised: August 11, 2017

Published: September 1, 2017

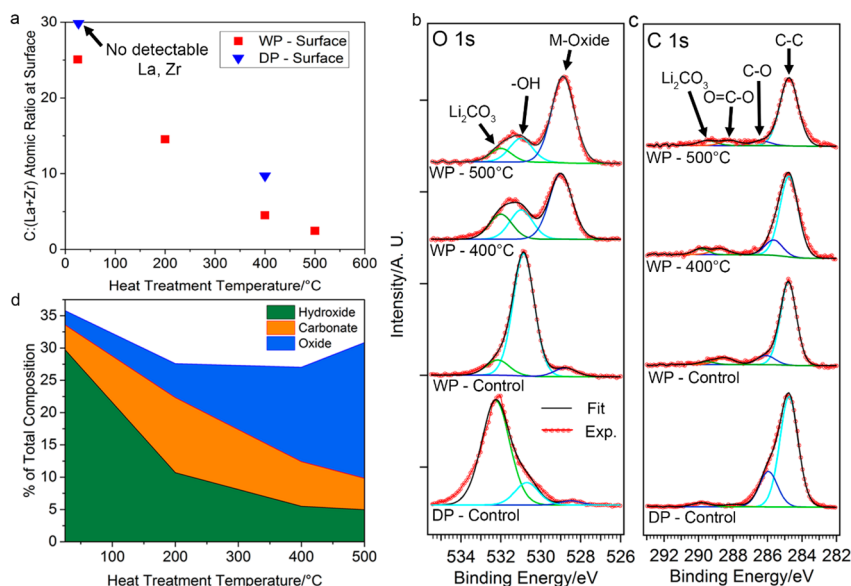


Figure 1. XPS analysis of LLZO before and after heat treatment at 400 and 500 °C. (a) C:(La+Zr) atomic ratio as a function of heat treatment temperature; (b) O 1s and (c) C 1s core levels; (d) percentage of total composition of different oxygen species on the LLZO surface as a function of heat treatment temperature after wet polishing (WP).

In this study, we provide a mechanistic understanding of the interplay between interfacial chemistry and electrochemical performance at solid–solid interfaces in SSBs. This understanding provides design rules for engineering low-resistance interfaces. Accordingly, we demonstrate that the Li–LLZO interfacial resistance can be nearly eliminated ($2 \Omega \text{ cm}^2$) through a simple, coating-free process to modify the surface chemistry of LLZO.

The importance of Li wettability in achieving low-resistance Li–SSE interfaces in SSBs has been discussed in a few recent studies.^{8–11} However, a quantitative evaluation of Li wettability as a function of SSE surface chemistry is currently lacking. To address this, molten Li contact angle measurements using a sessile drop test were conducted on several relevant surfaces including LLZO with varying surface chemistry. Trends in the measured contact angles are consistent with those calculated with density functional theory (DFT) and demonstrate the connection between surface chemistry and Li wettability.

Our study quantitatively demonstrates the relationships between interfacial chemistry, lithium wettability, and facile charge transport. Equipped with this understanding, we demonstrate that controlling interfacial chemistry enables a straightforward pathway toward viable SSBs.

RESULTS AND DISCUSSION

Surface Chemical Analysis. As has previously been shown, the surface chemistry of LLZO is sensitive to air exposure.^{7,12} A contamination layer readily forms and is predominantly composed of lithium carbonate (Li_2CO_3), lithium hydroxide (LiOH), and other adventitious carbon species,^{7,12} which collectively result in high interfacial resistance between LLZO and metallic Li.^{7,13} It has been reported that dry polishing in an inert atmosphere can lower the interfacial resistance by partially cleaning the surface; however, the efficacy of this approach is limited to reducing the interface resistance from $\sim 1000 \Omega \text{ cm}^2$ to $\sim 100 \Omega \text{ cm}^2$.^{7,13} Here, several surface conditioning protocols, including dry polishing (DP), wet polishing (WP), and heat treatments (HT), were employed in

an attempt to reduce the interfacial resistance, and their impact on LLZO surface chemistry was evaluated (details regarding the dry and wet polishing conditions are explained in the [Experimental Section](#)). Heat treatment between 200 and 500 °C in an inert atmosphere was conducted after dry and wet polishing.

The surface chemistry of LLZO was analyzed using X-ray photoelectron spectroscopy (XPS) after each conditioning protocol ([Figure 1](#)). Measurements were performed on samples transferred without air exposure between an argon-filled glovebox and the ultrahigh vacuum XPS chamber. [Figure 1a](#) shows that in samples conditioned with DP or WP (no HT) a surface layer blocks nearly all the signal attributed to La and Zr. In these cases, the surface layer is composed almost entirely of H, Li, C, and O (H content cannot be directly detected by XPS but can be observed as hydroxyl bonds). The nature of the bonds in which these species participate can be examined through high-resolution core-scans. The O 1s peak reveals a significant difference between the surface layer after wet versus dry polishing ([Figure 1b](#)). The WP surface consists of predominantly hydroxide species, while a greater concentration of carbonate species exists on the DP sample. This suggests that the use of polishing fluid protects the LLZO surface from reformation of carbonate species.

Samples that underwent HT were first polished (DP or WP in ambient air) and then immediately transferred into an argon-filled glovebox where the samples were heated to different temperatures. Subsequent XPS analysis demonstrated significant variations in the surface chemistry of these samples. In [Figure 1a](#), a plot of the ratio of the C content to the summed La and Zr contents is used as a metric to quantify the amount of surface contamination. The lower the ratio, the more closely the surface resembles bulk LLZO. Some adventitious carbon is always observed on the LLZO surface, even for samples kept continuously in an argon atmosphere after HT, [Figure 1c](#). The amount of contamination is observed to dramatically decrease after heating to 400 and 500 °C. This is consistent with the O 1s core scans shown for these samples, which demonstrate that

the predominantly hydroxide and carbonate surfaces before heating are converted to primarily oxide species (as expected in bulk LLZO) after heating (Figure 1b). In contrast, heating a DP sample to 400 °C did not change the surface as dramatically, with carbonate species still dominating (Figure S1). A plot of the fractional surface composition of the oxygen-containing species is shown in Figure 1d for WP samples heated to different temperatures. As the HT temperature increases to 500 °C, the oxide fraction steadily increases, the hydroxide fraction decreases, and the amount of carbonate remains roughly constant. In total, these observations suggest that (1) compared to dry polishing, wet polishing is more effective at achieving a surface with low carbonate content, (2) heat treatment up to 500 °C can remove LiOH but is less effective at removing Li_2CO_3 , and (3) of the strategies examined, the successive combination of WP and HT is the most effective at removing both carbonate and hydroxide surface contamination layers.

The removal of LiOH species at temperatures between 400 and 500 °C is consistent with prior thermogravimetric analysis, mass spectroscopy, and first-principles calculations.^{13,14} This suggests that the surface layer that reforms as a result of wet polishing is more easily removed by HT, thereby making the combination of wet polishing and HT in an inert atmosphere an attractive option to achieve a well-controlled LLZO surface prior to forming the Li–LLZO interface.

Contact Angle Measurements and Calculations. The wettability of a SSE by metallic Li has been proposed to influence interfacial resistance in SSBs.^{8,9,11,15,16} However, quantitative analysis of the Li contact angle and direct correlation with surface chemistry have not been reported. To characterize wettability, sessile drop tests were performed to measure the contact angle of molten Li on Li_2CO_3 and on LLZO samples after various surface conditioning processes (Figure 2). Molten Li was deposited onto heated Li_2CO_3 or LLZO from a heated stainless-steel syringe. Both the surfaces and the syringe were kept above the Li melting temperature. Importantly, the native layers (composed of oxide, nitride, and carbonate species)¹⁷ present on the surface of the Li foil did not

melt and thus were easily removed from the molten Li source. This allowed for deposition of purified molten Li onto the LLZO surface. The present approach differs from a scenario involving the melting of solid Li foil directly on LLZO, as wettability in the latter approach will be influenced by the presence of native layers on the Li surface and at the Li–LLZO interface. All experiments were performed inside an argon-filled glovebox, and high-resolution cross-sectional images were captured and digitally analyzed to determine contact angles.

As shown in Figure 2, the DP-LLZO sample exhibited the highest contact angle among all LLZO samples, $\theta = 146^\circ$, which was nearly identical to the value measured for a pure Li_2CO_3 surface ($\theta = 142^\circ$). Such a large contact angle is consistent with a nonwetting interaction typical of an interface exhibiting weak adhesion. The similar wetting behavior observed for both the DP-LLZO sample and Li_2CO_3 is expected, given that the DP-LLZO surface is composed predominantly of Li_2CO_3 . Similarly, the WP-LLZO contact angle was 141° , which is consistent with the presence of the hydroxide and carbonate contamination layer, which was observed with XPS. **Supplementary Videos 1 and 2** demonstrate the similarly lithiophobic nature of Li_2CO_3 and DP-LLZO as molten Li easily rolls off these surfaces. In contrast, the WP-LLZO, heat treated at 500 °C, exhibited a significantly lower contact angle ($\theta = 95^\circ$). We hypothesize that this reduction in contact angle is caused by the removal of hydroxide and carbonate species, resulting in a surface more closely resembling bulk LLZO, which interacts more strongly with Li metal. **Supplementary Video 3** demonstrates the more lithiophilic nature of this interface, as molten Li maintains adherence to the LLZO surface even when fully inverted vertically.

To validate the correlation between surface chemistry and wettability, the wetting angle of Li on LLZO, Li_2CO_3 , and LiOH was evaluated using DFT calculations.¹⁸ Li–LLZO, Li– Li_2CO_3 , and Li–LiOH interfaces were constructed from the low-energy surfaces of each respective material, as reported previously.^{16,19,20} Large simulation cells were used to accommodate geometries that minimize interfacial strain. The interfacial distance and translation state within the interfacial plane were optimized to identify the most energetically favorable interface structures.

Figure 3 shows the atomic structure of the low-energy interfaces for Li–LLZO and Li– Li_2CO_3 (data for Li–LiOH are shown in Table S2). The contact angle, θ , for these interfaces was calculated by combining the Young–Dupré equation, $W_{\text{ad}} = \sigma_{\text{Li}} (1 + \cos \theta)$, with DFT calculations of the interfacial work of adhesion, W_{ad} , and the surface energy of Li, $\sigma_{\text{Li}} = 0.45 \text{ J m}^{-2}$. Using the Li–LLZO interface as an example, W_{ad} was evaluated as $W_{\text{ad}} = E_{\text{int}} - E_{\text{Li-slab}} - E_{\text{LLZO-slab}}$. Here, E_{int} is the energy of the interface cell and $E_{\text{X-slab}}$ refers to the energy of an isolated Li (X = Li) or LLZO slab (X = LLZO). The calculated values for W_{ad} and θ are shown in Figure 3 below their respective interfaces. The trend predicted by our calculations—that Li strongly wets LLZO, but not Li_2CO_3 , is consistent with the measurements shown in Figure 2. More specifically, the wetting angle predicted for the Li– Li_2CO_3 interface, $\theta = 142^\circ$, is in excellent agreement with the measured value (142° , Figure 2a) indicating a weak interfacial interaction between Li and Li_2CO_3 ($W_{\text{ad}} = 0.10 \text{ J m}^{-2}$). In contrast, the calculated W_{ad} for the Li–LLZO interface is nearly seven times larger, $W_{\text{ad}} = 0.67 \text{ J m}^{-2}$, resulting in a relatively small wetting angle, $\theta = 62^\circ$. This value is qualitatively consistent with the measured value of 95° reported

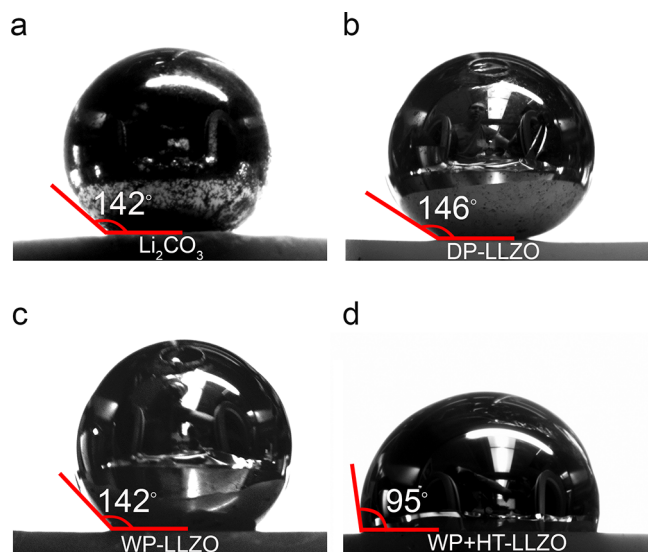


Figure 2. Contact angle measurements of molten metallic Li on (a) Li_2CO_3 , (b) DP-LLZO, (c) WP-LLZO, (d) WP-LLZO after heat treatment at 500 °C.

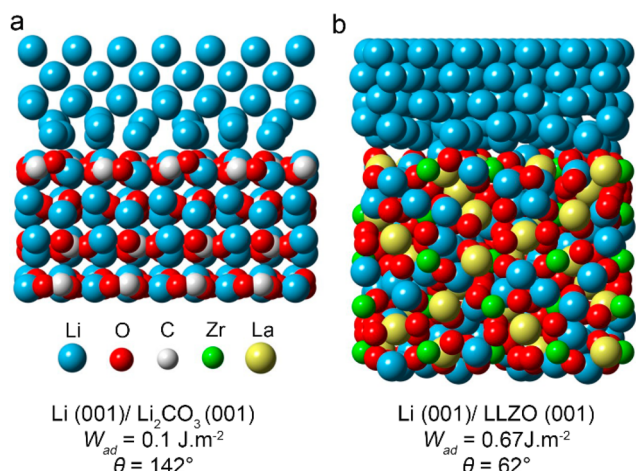


Figure 3. Calculated work of adhesion (W_{ad}), contact angle (θ), and atomic structure for the (a) Li–Li₂CO₃ and (b) Li–LLZO interfaces.

in Figure 2d. The smaller value predicted by our calculations is expected, given that approximately 15% of carbonate or hydroxide remains on the LLZO surface after heating to 500 °C (Figure 2d). Calculations on the Li–LiOH interface predict a relatively large contact angle of 125°, similar to the nonwetting behavior observed for the Li–Li₂CO₃ system (see Table S2).

Electrochemical Characterization. Electrochemical impedance spectroscopy (EIS) was performed on Li–LLZO–Li symmetric cells (Figure 4a) to measure the LLZO bulk (R_{bulk}), grain boundary (R_{gb}), and Li–LLZO interfacial ($R_{Li-LLZO}$) resistances for WP and HT samples between 200 and 500 °C. EIS data were modeled using an equivalent circuit shown in Figure 4b. This approach allowed for the direct measurement of

the individual contributions to cell resistance and involves the correlation between characteristic frequencies and transport phenomena.²¹ Representative EIS spectra for a cell consisting of a WP and HT at 500 °C LLZO sample before and after preconditioning at 175 °C are shown in Figure 4c (preconditioning was used to ensure good contact between metallic Li and LLZO by heating the Li–LLZO–Li cell to 175 °C for 12 h).⁶ From Figure 4c, it is apparent the LLZO total resistance ($R_{bulk} + R_{gb}$) has remained constant (500 Ω cm²), while $R_{Li-LLZO}$ dramatically decreased upon preconditioning at 175 °C and cooling. Initially, $R_{Li-LLZO}$ was approximately 400 Ω cm², which is significantly lower than previous values reported for LLZO after dry polishing in literature.⁶ After preconditioning at 175 °C, a further dramatic reduction in $R_{Li-LLZO}$ was observed. The combination of wet polishing, HT, and preconditioning results in an extremely small interfacial resistance of 2 Ω cm².

Figure 4d shows $R_{Li-LLZO}$ after preconditioning for WP LLZO samples with no HT and HT at several temperatures between 200 and 500 °C. With increasing HT temperature, $R_{Li-LLZO}$ decreases from 400 to 2 Ω cm². Importantly, the low interfacial resistance coincides with the removal of the surface contamination layer. Furthermore, the decrease in interfacial resistance closely follows the trend in surface chemistry with HT temperature observed in XPS measurements, and with the improved wettability of the LLZO surface after HT. Taken together, these observations provide quantitative evidence of the strong coupling between surface chemistry, wettability, and interfacial resistance.

The cycling behavior and critical current density (CCD) of a WP-LLZO sample HT to 500 °C (WP+HT) were characterized using a combination of DC cycling and EIS analysis (Figure 5). The CCD is defined as the lowest current density at which cell shorting occurs due to Li metal penetration.^{6,22} After

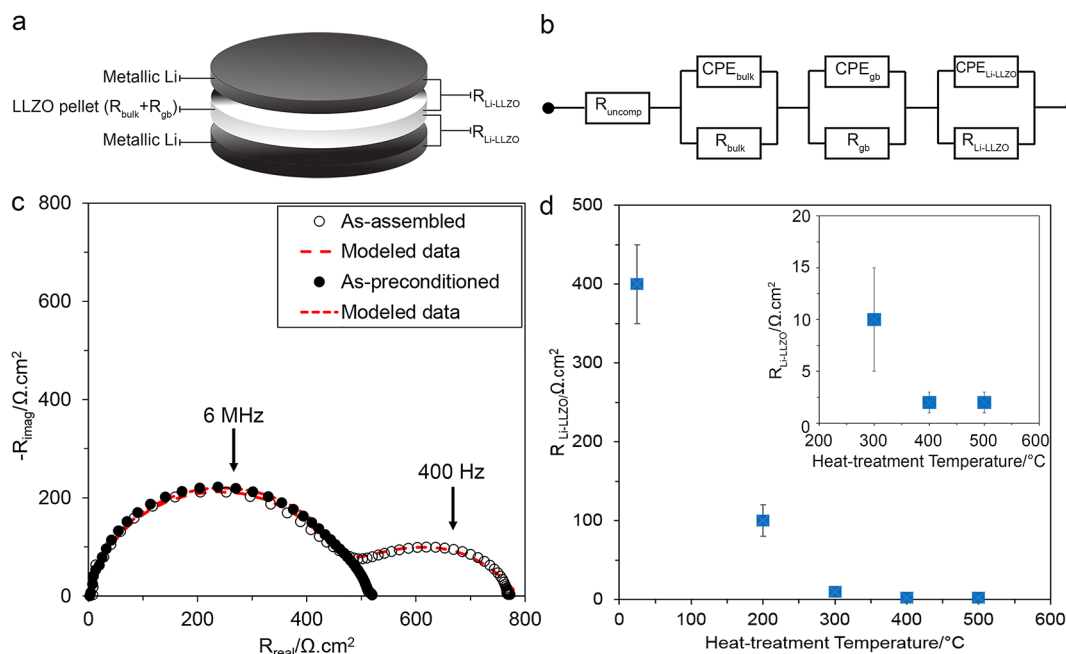


Figure 4. (a) Schematic of the all solid-state Li–LLZO–Li cell, (b) equivalent circuit used for modeling the EIS data, (c) representative Nyquist plot of the Li–LLZO–Li cell (for LLZO heat-treated at 500 °C), as-assembled (○) and after preconditioning at 175 °C (●). Markers indicate experimental data and dotted lines represent from the equivalent circuit model simulation using the circuit shown in panel b, (d) the Li–LLZO interfacial resistance after preconditioning at 175 °C versus the heat-treatment temperature. $N = 3$ for each HT condition. Error bars represent standard deviations.

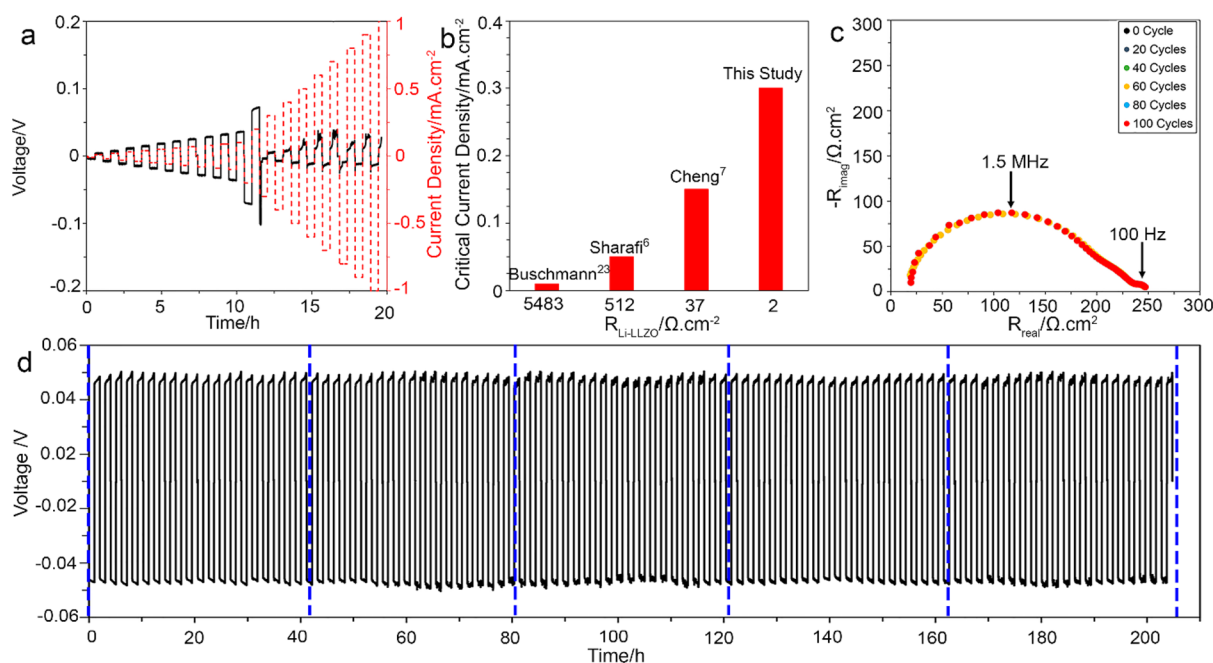


Figure 5. (a) DC cycling of Li–LLZO–Li cells (LLZO HT to 500 °C after WP) at room temperature, stepping the current density from 0.01 to 1 mA cm⁻², (b) the critical current density versus Li–LLZO interfacial resistance comparing the results of this study with other studies available in the literature, (c) Nyquist plots of a Li–LLZO–Li cell after each 20 cycles for cell cycled 100 times, (d) galvanostatic cycling of Li–LLZO–Li at 0.2 mA cm⁻² for 100 cycles at 0.4 mAh cm⁻². The blue dotted line shows the times at which EIS was collected and is shown in panel c.

removal of the surface contamination, the CCD was determined to be 0.3 mA cm⁻² (Figure 5a). The CCD from the WP+HT sample prepared here is compared in Figure 5b to other Li–LLZO–Li symmetric cells reported in the literature.^{6,7,23} The CCD measured in this study is one of the highest values reported in literature for an LLZO SSE. Our data indicate that the CCD and $R_{\text{Li-LLZO}}$ are inversely correlated, suggesting that higher power density can be achieved by controlling interfacial chemistry, and thus $R_{\text{Li-LLZO}}$.

To evaluate the stability of the interface after WP+HT upon cycling, a Li–LLZO–Li cell was cycled for one hundred cycles at ± 0.2 mA cm⁻² at room temperature (Figure 5d). After every 20 cycles, EIS analysis was conducted to assess changes in R_{bulk} , R_{gb} , and $R_{\text{Li-LLZO}}$. Figure 5c shows that negligible changes in the EIS spectra were observed, implying excellent stability of the interface and the absence of short-circuiting. Furthermore, the total cell resistance ($R_{\text{bulk}} + R_{\text{gb}} + R_{\text{Li-LLZO}}$) estimated using the DC cell polarization voltage (230 Ω cm²) (Figure 5a) agrees well with the total cell resistance measured using EIS (240 Ω cm²). This agreement further validates the interpretation of the EIS data.

The DC and EIS characterization illustrate the importance of controlling interfacial chemistry. First, a low $R_{\text{Li-LLZO}}$ enables a path toward low resistance solid-state cell designs employing metallic Li anodes. Second, reducing $R_{\text{Li-LLZO}}$ increases the CCD. Although 0.3 mA cm⁻² is one of the highest reported CCD values, it must be further increased to demonstrate relevance to vehicle electrification; the data in Figure 5b suggest further tuning surface chemistry and reducing $R_{\text{Li-LLZO}}$ may be an approach to achieve higher CCD. Lastly, a clean and discrete Li–LLZO interface is preferred to minimize side reactions and mechanical degradation. In preliminary cycling tests, the interface kinetics appear to be stable when cycling at ± 0.2 mA cm⁻² at room temperature. Altogether, the electrochemical

characterization suggests WP+HT could enable the use of metallic Li anodes and LLZO in SSBs.

CONCLUSIONS

In closing, this study reveals the mechanism by which surface chemistry controls the resistance of the Li–LLZO interface. By exploiting this mechanism, very low interfacial resistances, 2 Ω cm⁻², comparable to solid–liquid interfaces in Li-ion cells, can be achieved without the need for coatings. The removal of LLZO surface contamination was demonstrated to enhance Li wetting of LLZO, which was quantitatively evaluated using molten Li contact angle measurements through sessile drop tests. The interfacial chemistry and wettability measurements agree with atomic-scale DFT calculations of interfacial adhesion and wetting angle. The effects of surface chemistry and wettability were quantitatively correlated with the Li–LLZO interfacial resistance. The lower interfacial resistance made possible by controlling surface chemistry resulted in a doubling of the critical current density. Moreover, this low interfacial resistance was preserved for one hundred cycles with no sign of short circuiting. This study clarifies the relationships between interfacial chemistry, lithium wettability, interfacial resistance, and stable cycling. The knowledge gained enables the rational design of electrode/electrolyte interfaces and has general implications for solid-state transport phenomena.

EXPERIMENTAL SECTION

LLZO Specimen Preparation. Cubic Al-doped LLZO with nominal composition of $\text{Li}_{6.25}\text{Al}_{0.25}\text{La}_3\text{Zr}_2\text{O}_{12}$ was prepared using solid-state synthetic technique.¹³ The methodology has been explained elsewhere in more detail. The calcined powder was densified using a custom rapid induction hot-press (RIHP) at 1100 °C and 62 MPa for 1 h in graphite dies under argon shielding gas to achieve >97% relative density. Each sample was cut into 1 ± 0.2 mm discs using a slow speed diamond saw. The discs were dry polished using 400 grit SiC sandpaper in air to ensure the parallel faces.

Surface Conditioning. Various surface conditioning processes including dry polishing (DP), wet polishing (WP), and heat treatment (HT) were used. For DP, LLZO samples were polished manually using 400, 600, and 1200 grit sandpaper (Norton Corporation) in air without polishing fluid. For WP, an automated polisher (EcoMet 300 Pro, Buehler) was used. First, LLZO samples were ground using 1200 sand paper (Norton Corporation). After grinding, the samples were polished on Technotron polishing cloth (Leco Corporation) loaded with glycol-based diamond paste extender as the polishing fluid (Leco Corporation) and diamond polishing abrasives. The diamond polishing abrasive sequence ranged from 15, 6, 1 and down to 0.5 μm . After each diamond abrasive, samples were rinsed with ethanol to remove the residual polishing fluid from surface. Immediately after polishing, samples were transferred to an argon-filled glovebox. Heat treatment (HT) was conducted by placing the samples in a MgO boat and heating to temperatures between 200 to 500 $^{\circ}\text{C}$ in 100 $^{\circ}\text{C}$ intervals in a muffle furnace (MTI Corporation) for 180 min using 4 $^{\circ}\text{C min}^{-1}$ as heating and cooling rate.

Surface Chemistry Characterization. A Kratos Axis Ultra was used for all XPS experiments. A custom O-ring sealed airtight transfer device was used to transfer samples into the XPS tool without air exposure. Survey scans used a pass energy of 160 eV and were quantified using Shirley backgrounds and Kratos sensitivity factors for the La 3d, Zr 3p, C 1s, O 1s, and Li 1s peaks in Casa XPS. Core scans used a pass energy of 20 eV and were energy calibrated using the C–C bond energy at 284.8 eV. The O 1s peak was fitted with three species, LiOH at 531.1 eV,²⁴ Li_2CO_3 at 532 eV,²⁵ and oxide species at 528.6–529 eV.²⁵ The C 1s peak was fitted with four species, adventitious carbon at 284.8 eV, which was used to calibrate the spectra, C–O at ~ 286 eV,²⁶ O–C=O at 289 eV,²⁷ and Li_2CO_3 at 290 eV.²⁵

Contact Angle Measurements. Li foil was melted in a crucible by heating on a hot plate in the glovebox. While melting, a thin film of impurities, likely composed of oxide, nitride, and carbonate species that originate from the native surface layers of the bulk foil, was observed to form on the top of the molten Li. The film was removed from the molten Li source using tweezers and a razor blade. This process was repeated until no surface layer was apparent, and the molten Li was purely liquid phase. Cold-pressed Li_2CO_3 and LLZO with various surface treatments were placed on a hot plate at 300 $^{\circ}\text{C}$ inside an argon-filled glovebox to ensure the sample temperature was higher than melting temperature of Li (>180 $^{\circ}\text{C}$). Subsequently, molten Li was injected on the surface with a stainless-steel syringe. The stainless-steel syringe was also heated to $T > 180$ $^{\circ}\text{C}$ to avoid solidification of molten Li. The contact angle measurement was performed by determining the tangent angle of the Li liquid drop with the sample surface. In this method, the shape of a droplet resting on a solid surface is dependent on the mechanical equilibrium of the drop under the three interfacial tensions including; solid–vapor (γ_{SV}), solid–liquid (γ_{SL}), and liquid–vapor (γ_{LV}). This is described by the Young–Dupree’s equation.²⁸ A high-resolution camera (Grasshopper GRAS-SO5SM-C) with a Fujinon HF75SA-1 lens was used to capture the image and measure contact angles. The contact angle plugin tool in ImageJ software was used to measure the contact angle.

DFT Calculations. First-principles calculations were performed using density functional theory (DFT) with a plane wave basis set and the projector augmented wave (PAW) method,²⁹ as implemented in the Vienna ab initio Simulation Package (VASP).¹⁸ The semilocal generalized gradient approximation (GGA) of Perdew, Burke, and Ernzerhof (PBE)³⁰ was used for the exchange–correlation energy. For LiOH, van der Waals-aware density functional (vdW-DF2)³¹ was additionally used to describe the weak interaction between LiOH (001) layers. An energy cutoff of 450 eV was used for the plane wave basis. The Brillouin zone was sampled using the Monkhorst–Pack scheme,³² with $3 \times 3 \times 1$, $4 \times 4 \times 1$, and $4 \times 4 \times 1$ k-point meshes used for the Li–LLZO, Li– Li_2CO_3 , and Li–LiOH interfaces, respectively. The convergence criterion for the electronic self-consistency loop was set to 10^{-5} eV, while atomic positions were relaxed until atomic forces were less than 0.05 eV \AA^{-1} .

The optimal lattice parameters for bulk cells were obtained by fitting total energy versus volume data to the Murnaghan equation of

state,³³ as shown in Table S1. The LLZO slab was constructed based on the cubic polymorph with partial occupancies of 0.542 and 0.448 on the 24 d and 96 h Li-sublattice sites, respectively.³ A (001) Li slab with 20 layers was used to calculate the surface energy of Li, which resulted in 0.452 J m^{-2} . The Li–LLZO, Li– Li_2CO_3 , and Li–LiOH interfaces were assembled using geometries that minimize interfacial strain; periodic boundary conditions in directions parallel to the interfacial plane were accommodated by adjusting the lattice constants of Li to match the dimensions of LLZO, Li_2CO_3 , or LiOH. The number of atoms in the interface supercell, the lattice parameters for the interface, and the in-plane strain of Li are listed in Table S2 for all three interface systems. A vacuum layer of 8 \AA was included in the interface supercells; each supercell contained one interface. The interfacial distance was determined by rigidly displacing the two slabs along the interface normal, and fitting the resulting energy versus displacement data to the Universal Binding Energy Relation (UBER).³⁴ This procedure resulted in minimum-energy interfacial distances of 1.96, 3.04, and 2.32 \AA for Li–LLZO, Li– Li_2CO_3 , and Li–LiOH, respectively. Ionic relaxations were then performed for the three interfaces starting from interfacial separations predicted by the UBER fit. For the Li–LLZO interface, which had the largest supercell size (570 atoms), atoms in the “back” half of each slab (i.e., the portion farthest from the interface) were fixed at their bulk-like positions. The Li– Li_2CO_3 and Li–LiOH interfaces were fully relaxed without fixing any atom positions. Testing on these two systems revealed that the work of adhesion was not strongly influenced by the presence/absence of these constraints.

The optimization of the translation state within the interfacial plane and the interfacial distance for the Li–LLZO and Li– Li_2CO_3 interfaces are shown in Figures S2 and S3, respectively. Contour plots of W_{ad} were obtained by translating the Li slab among many configurations at a constant interfacial distance. The lowest interface in the contour plot was then used to calculate interfacial distance by fitting to the UBER. For LiOH, the values of W_{ad} upon translating the Li slab were nearly identical. Optimization of the interfacial distance for the Li–LiOH interface using the UBER is shown in Figure S4.

Electrochemical Measurements. Electrochemical measurements were performed to determine the effect of HT on $R_{\text{Li–LLZO}}$ and the maximum critical current density (CCD). Metallic Li electrodes were prepared by scraping with a stainless-steel spatula to expose a clean surface. Li–LLZO–Li cells were compressed under a constant 350 kPa uniaxial pressure during cycling. EIS measurements were conducted on symmetric cells after assembly using a 100 mV amplitude in the frequency range of 7 MHz to 1 Hz using a VMP-300 biologic and EC-Lab V11.02 software. To ensure good contact between metallic Li and LLZO, cells were heated to 175 $^{\circ}\text{C}$ for 12 h as has been reported by Sharafi et al. (preconditioning step).⁶ After cooling to room temperature, the change in cell resistance with a focus on $R_{\text{Li–LLZO}}$ was measured by EIS again. First, the entire spectrum was normalized for the contact area between Li and LLZO (area = 1.26 cm^2). Then an equivalent circuit model was used to interpret the data. The EIS data were modeled using the equivalent circuit model shown in Figure 4b. In this model, a combination of a resistor and a capacitor in parallel was used to represent each transport phenomenon in the cell. Thus, three parallel combinations were used in the model representing the bulk (R_{bulk}), the grain boundary (R_{gb}), and the Li–LLZO interface ($R_{\text{Li–LLZO}}$). Ideal capacitors were replaced with constant phase elements (CPE) to account for any nonideal behavior and dispersion in the time constant. The ideality of the CPE is represented by the coefficient α ($\alpha = 1$ shows the component is behaving as an ideal capacitor).³⁵ The Q values for the CPE should be on the order of 10^{-12} , 10^{-8} , 10^{-6} F for bulk, grain boundary, and Li–LLZO interface, respectively.^{35,36}

Cycling behavior of Li–LLZO–Li symmetric cells was measured at room temperature between 0.01 and 1 mA cm^{-2} to determine the CCD (the current density at which the cell voltage dropped to 0 V). Cycling was continued until evidence of short-circuiting was observed and marked by a sudden drop in polarization voltage. To examine the cycling behavior of LLZO, Li–LLZO–Li cells were galvanostatically cycled at ± 0.2 mA cm^{-2} . During cell cycling, the cell impedance was

measured every 20 cycles to evaluate the impact of electrochemical cycling on cell impedance and its stability. In this study, all tests have been repeated three times to ensure reproducibility.

■ ASSOCIATED CONTENT

● Supporting Information

The Supporting Information is available free of charge on the ACS Publications website at DOI: 10.1021/acs.chemmater.7b03002.

XPS results for dry-polished LLZO before and after heat treatment; further details about DFT calculations (PDF)
Li wettability on lithium carbonate (AVI)
Li wettability on dry-polished LLZO (AVI)
Li wettability on wet-polished and heat-treated LLZO (AVI)

■ AUTHOR INFORMATION

Corresponding Authors

*E-mail: jeffsaka@umich.edu.

*E-mail: ndasgupta@umich.edu.

ORCID

Asma Sharafi: 0000-0001-7809-579X

Seungho Yu: 0000-0003-3912-6463

Travis Thompson: 0000-0003-3178-3346

Donald J. Siegel: 0000-0001-7913-2513

Neil P. Dasgupta: 0000-0002-5180-4063

Author Contributions

A.S. and E.K. contributed equally to this work.

Notes

The authors declare no competing financial interest.

■ ACKNOWLEDGMENTS

A.S., S.Y., D.J.S., and J.S. acknowledge support from the U.S. Department of Energy Advanced Battery Material Research (BMR) program, Grant No. DE-EE-00006821. E.K. acknowledges support from a National Science Foundation Graduate Research Fellowship under Grant No. DGE 1256260. S.Y. acknowledges support from the Kwanjeong Educational Foundation.

■ REFERENCES

- (1) Tarascon, J.-M.; Armand, M. Issues and Challenges Facing Rechargeable Lithium Batteries. *Nature* **2001**, *414*, 359–367.
- (2) Van Noorden, R. A Better Battery. *Nature* **2014**, *507*, 26–28.
- (3) Yu, S.; Schmidt, R. D.; Garcia-Mendez, R.; Herbert, E.; Dudney, N. J.; Wolfenstine, J. B.; Sakamoto, J.; Siegel, D. J. Elastic Properties of the Solid Electrolyte $\text{Li}_7\text{La}_3\text{Zr}_2\text{O}_{12}$ (LLZO). *Chem. Mater.* **2016**, *28*, 197–206.
- (4) Murugan, R.; Thangadurai, V.; Weppner, W. Fast Lithium Ion Conduction in Garnet-Type $\text{Li}_7\text{La}_3\text{Zr}_2\text{O}_{12}$. *Angew. Chem., Int. Ed.* **2007**, *46*, 7778–7781.
- (5) Zhang, S.; Xu, K.; Jow, T. The Low Temperature Performance of Li-Ion Batteries. *J. Power Sources* **2003**, *115*, 137–140.
- (6) Sharafi, A.; Meyer, H. M.; Nanda, J.; Wolfenstine, J.; Sakamoto, J. Characterizing the $\text{Li}-\text{Li}_7\text{La}_3\text{Zr}_2\text{O}_{12}$ Interface Stability and Kinetics as a Function of Temperature and Current Density. *J. Power Sources* **2016**, *302*, 135–139.
- (7) Cheng, L.; Chen, W.; Kunz, M.; Persson, K.; Tamura, N.; Chen, G.; Doeff, M. Effect of Surface Microstructure on Electrochemical Performance of Garnet Solid Electrolytes. *ACS Appl. Mater. Interfaces* **2015**, *7*, 2073–2081.
- (8) Tsai, C.-L.; Roddatis, V.; Chandran, C. V.; Ma, Q.; Uhlenbruck, S.; Bram, M.; Heitjans, P.; Guillon, O. $\text{Li}_7\text{La}_3\text{Zr}_2\text{O}_{12}$ Interface

Modification for Li Dendrite Prevention. *ACS Appl. Mater. Interfaces* **2016**, *8*, 10617–10626.

(9) Han, X.; Gong, Y.; Fu, K. K.; He, X.; Hitz, G. T.; Dai, J.; Pearce, A.; Liu, B.; Wang, H.; Rubloff, G.; et al. Negating Interfacial Impedance in Garnet-Based Solid-State Li Metal Batteries. *Nat. Mater.* **2016**, *16*, 572–579.

(10) Fu, K. K.; Gong, Y.; Liu, B.; Zhu, Y.; Xu, S.; Yao, Y.; Luo, W.; Wang, C.; Lacey, S. D.; Dai, J.; et al. Toward Garnet Electrolyte-Based Li Metal Batteries: An Ultrathin, Highly Effective, Artificial Solid-State Electrolyte/Metallic Li Interface. *Sci. Adv.* **2017**, *3*, e1601659.

(11) Wang, C.; Gong, Y.; Liu, B.; Fu, K. K.; Yao, Y.; Hitz, E.; Li, Y.; Dai, J.; Xu, S.; Luo, W.; et al. Conformal, Nanoscale ZnO Surface Modification of Garnet-Based Solid State Electrolyte for Lithium Metal Anodes. *Nano Lett.* **2017**, *17*, 565–571.

(12) Larraz, G.; Orera, A.; Sanjuan, M. Cubic Phases of Garnet-Type $\text{Li}_7\text{La}_3\text{Zr}_2\text{O}_{12}$: The Role of Hydration. *J. Mater. Chem. A* **2013**, *1*, 11419–11428.

(13) Sharafi, A.; Yu, S.; Naguib, M.; Lee, M.; Ma, C.; Meyer, H. M.; Nanda, J.; Chi, M.; Siegel, D. J.; Sakamoto, J. Impact of Air Exposure and Surface Chemistry on $\text{Li}-\text{Li}_7\text{La}_3\text{Zr}_2\text{O}_{12}$ Interfacial Resistance. *J. Mater. Chem. A* **2017**, *5*, 13475–13478.

(14) Beyer, H.; Meini, S.; Tsiouvaras, N.; Piana, M.; Gasteiger, H. Thermal and Electrochemical Decomposition of Lithium Peroxide in Non-Catalyzed Carbon Cathodes for Li–Air Batteries. *Phys. Chem. Chem. Phys.* **2013**, *15*, 11025–11037.

(15) Luo, W.; Gong, Y.; Zhu, Y.; Li, Y.; Yao, Y.; Zhang, Y.; Fu, K. K.; Pastel, G.; Lin, C. F.; Mo, Y.; et al. Reducing Interfacial Resistance between Garnet-Structured Solid-State Electrolyte and Li-Metal Anode by a Germanium Layer. *Adv. Mater.* **2017**, *29*, 1606042.

(16) Liu, Z.; Qi, Y.; Lin, Y.; Chen, L.; Lu, P.; Chen, L. Interfacial Study on Solid Electrolyte Interphase at Li Metal Anode: Implication for Li Dendrite Growth. *J. Electrochem. Soc.* **2016**, *163*, A592–A598.

(17) Kanamura, K.; Tamura, H.; Takehara, Z. i XPS Analysis of a Lithium Surface Immersed in Propylene Carbonate Solution Containing Various Salts. *J. Electroanal. Chem.* **1992**, *333*, 127–142.

(18) Kresse, G.; Furthmüller, J. Efficient Iterative Schemes for Ab Initio Total-Energy Calculations Using a Plane-Wave Basis Set. *Phys. Rev. B: Condens. Matter Mater. Phys.* **1996**, *54*, 11169–11186.

(19) Thompson, T.; Yu, S.; Williams, L.; Schmidt, R. D.; Garcia-Mendez, R.; Wolfenstine, J.; Allen, J. L.; Kioupakis, E.; Siegel, D. J.; Sakamoto, J. Electrochemical Window of the Li-ion Solid Electrolyte $\text{Li}_7\text{La}_3\text{Zr}_2\text{O}_{12}$. *ACS Energy Lett.* **2017**, *2*, 462–468.

(20) Ling, C.; Zhang, R.; Takechi, K.; Mizuno, F. Intrinsic Barrier to Electrochemically Decompose Li_2CO_3 and LiOH. *J. Phys. Chem. C* **2014**, *118*, 26591–26598.

(21) Irvine, J. T.; Sinclair, D. C.; West, A. R. Electroceramics: Characterization by Impedance Spectroscopy. *Adv. Mater.* **1990**, *2*, 132–138.

(22) Cheng, E. J.; Sharafi, A.; Sakamoto, J. Intergranular Li Metal Propagation through Polycrystalline $\text{Li}_{6.25}\text{Al}_{0.25}\text{La}_3\text{Zr}_2\text{O}_{12}$ Ceramic Electrolyte. *Electrochim. Acta* **2017**, *223*, 85–91.

(23) Buschmann, H.; Dölle, J.; Berendts, S.; Kuhn, A.; Bottke, P.; Wilkening, M.; Heitjans, P.; Senyshyn, A.; Ehrenberg, H.; Lotnyk, A.; et al. Structure and Dynamics of the Fast Lithium Ion Conductor $\text{Li}_7\text{La}_3\text{Zr}_2\text{O}_{12}$. *Phys. Chem. Chem. Phys.* **2011**, *13*, 19378–19392.

(24) Dupin, J.-C.; Gonbeau, D.; Vinatier, P.; Levasseur, A. Systematic XPS Studies of Metal Oxides, Hydroxides and Peroxides. *Phys. Chem. Chem. Phys.* **2000**, *2*, 1319–1324.

(25) Yao, K. P.; Kwabi, D. G.; Quinlan, R. A.; Mansour, A. N.; Grimaud, A.; Lee, Y.-L.; Lu, Y.-C.; Shao-Horn, Y. Thermal Stability of Li_2O_2 and Li_2O for Li–Air Batteries: In Situ XRD and XPS Studies. *J. Electrochem. Soc.* **2013**, *160*, A824–A831.

(26) Huang, M.; Liu, T.; Deng, Y.; Geng, H.; Shen, Y.; Lin, Y.; Nan, C.-W. Effect of Sintering Temperature on Structure and Ionic Conductivity of $\text{Li}_{7-x}\text{La}_3\text{Zr}_2\text{O}_{12-0.5x}$ ($x = 0.5 \sim 0.7$) Ceramics. *Solid State Ionics* **2011**, *204–205*, 41–45.

(27) Jena, R. K.; Yue, C. Y. Cyclic Olefin Copolymer Based Microfluidic Devices for Biochip Applications: Ultraviolet Surface

Grafting Using 2-Methacryloyloxyethyl Phosphorylcholine. *Biomicrofluidics* **2012**, 6, 012822.

(28) Young, T. An Essay on the Cohesion of Fluids. *Philos. Trans. R. Soc. London* **1805**, 95, 65–87.

(29) Kresse, G.; Joubert, D. From Ultrasoft Pseudopotentials to the Projector Augmented-Wave Method. *Phys. Rev. B: Condens. Matter Mater. Phys.* **1999**, 59, 1758–1775.

(30) Perdew, J. P.; Burke, K.; Ernzerhof, M. Generalized Gradient Approximation Made Simple. *Phys. Rev. Lett.* **1996**, 77, 3865–3868.

(31) Lee, K.; Murray, E. D.; Kong, L.; Lundqvist, B. I.; Langreth, D. C. Higher-Accuracy Van Der Waals Density Functional. *Phys. Rev. B: Condens. Matter Mater. Phys.* **2010**, 82, 081101–1–081101–4.

(32) Monkhorst, H. J.; Pack, J. D. Special Points for Brillouin-Zone Integrations. *Phys. Rev. B* **1976**, 13, 5188–5193.

(33) Murnaghan, F. The Compressibility of Media under Extreme Pressures. *Proc. Natl. Acad. Sci. U. S. A.* **1944**, 30, 244–247.

(34) Smith, J. R.; Hong, T.; Srolovitz, D. J. Metal-Ceramic Adhesion and the Harris Functional. *Phys. Rev. Lett.* **1994**, 72, 4021–4024.

(35) Huggins, R. A. Simple Method to Determine Electronic and Ionic Components of the Conductivity in Mixed Conductors a Review. *Ionics* **2002**, 8, 300–313.

(36) Huggins, R. *Advanced Batteries: Materials Science Aspects*; Springer Science & Business Media, 2008.